mater.scichina.com link.springer.com

Sci China Mater 2025, 68(5): 1435–1444
https://doi.org/10.1007/s40843-024-3156-6

SPECIAL TOPIC: Photovoltaic Materials, Devices, and Applications

Roll-to-roll gravure printed organic solar cells based on low-cost polythiophene donor

Weitao Qi[1,2†], Xiyue Yuan[3†], Yuanqi Liu[2], Shutao Yang[2], Yunsha Chu[2], Fan Qian[2], Lingpeng Yan[1*], Zhenguo Wang[2*], Chunhui Duan[3*], Qun Luo[2*] and Chang-Qi Ma[2]

ABSTRACT Although the power conversion efficiency (PCE) of organic solar cells (OSCs) has exceeded 20%, the development of printed large-area low-cost OSCs is still lacking. For the realization of low-cost OSCs, the materials and the manufacturing method are two important factors. Regarding the materials, polythiophene polymer donor material is a cost-effective material. Regarding fabrication, gravure printing is a large-area preparation method that has the advantages of high-speed, high-precision, low-cost, and two-dimensional patternable. To achieve low-cost OSCs, flexible OSCs based on polythiophene donor materials are prepared through roll-to-roll (R2R) gravure printing in this work. On one side, the viscosity of the active layer ink is regulated by adjusting the concentration of the ink, which significantly suppresses the generation of flow stripes in the gravure printing film and obtains a uniform film. On the other side, the excessive aggregation of gravure-printed active layer film morphology is inhibited by controlling the temperature of the ink. Finally, 1 cm^2 flexible OSCs from R2R gravure printing show an efficiency of 10.55%, which is comparable to that of spin-coated devices. This study reveals that the low-cost polythiophene material system is suitable for fabrication through R2R gravure printing, which is expected to be applied in future low-cost OSCs.

Keywords: flexible OSCs, gravure printing, active layer, polythiophene, viscosity

INTRODUCTION

As an emerging high-efficiency solar cell, organic solar cells (OSCs) can be widely used in wearable electronics, portable power supplies, and building-integrated photovoltaics due to their advantages of light, flexible, roll-to-roll printing (R2R) and large-area fabrication compatible properties [1–3]. In recent years, due to the rapid development of new organic semiconductors [4–6], and the optimization of morphology [7–13] and interface engineering [14–17], the power conversion efficiency (PCE) of the small-area single-junction OSCs fabricated in the laboratory has exceeded 20% [18]. However, most of these high-efficiency devices are prepared by spin coating [19,20], which is not compatible with commercialization of the large-area thin films [21,22].

At present, the main large-area fabrication methods for OSCs include blade coating [23,24] and slot-die coating [25,26]. The blade coating process can fabricate large-area film with uniform morphology; however, it is not patternable [27,28]. The slot-die coating is a comparably one-dimensional (1D) patterning, but the pattern has an obvious edge effect, which seriously influences the aesthetics of OSCs module [27,29]. Compared with the coating routes, gravure printing [30–32] is a promising technology for large-area fabrication due to its advantages of high resolution, high speed, 2D patternable, and roll-to-roll (R2R) compatibility [27,33–35]. Gravure printing has been widely used in the field of packaging, banknotes, and other fields. In the felid of OSCs, Kopola *et al.* [36] fabricated P3HT:PC_{61}BM (P3HT: poly(3-hexylthiophene)) OSCs by gravure printing in 2011, and the device modules with areas of 9.65 cm^2, 13.51 cm^2 and 15.45 cm^2 gave PCEs of 1.92%, 1.79% and 1.68%, respectively. In 2015, Välimäki *et al.* [37] fabricated large-area OSC modules through gravure-printed and screen-printed methods, and the modular device PCE of 96.5 cm^2 P3HT:PC_{61}BM OSCs reached 2.1%. In 2017, Välimäki *et al.* [35] achieved the fabrication of 50 cm^2 OSCs with a leaf shape, and the module device PCE was 2.0%. Later, our group successfully fabricated silver nanowire (AgNW) electrodes [38], zinc oxide (ZnO) electron transporting layer [29], and PM6:BTP-BO-4Cl organic photoactive layer through R2R gravure printing. These studies demonstrate the great potential of the manufacture of large-area OSCs through gravure printing. Although the fully R2R (three-layer) printed OSCs with an area of 1.0 cm^2 show a PCE of 12.10% [39], the donor material PM6 is relatively expensive.

Polythiophenes is considered to be the most cost-effective and easily scalable donor material due to its simple chemical struc-

[1] College of Materials Science and Engineering, Taiyuan University of Technology, Taiyuan 030024, China
[2] i-Lab & Printable Electronics Research Center, Suzhou Institute of Nano-Tech and Nano-Bionics, Chinese Academy of Sciences (CAS), Suzhou 215123, China
[3] Institute of Polymer Optoelectronic Materials and Devices, Guangdong Basic Research Center of Excellence for Energy & Information Polymer Materials, State Key Laboratory of Luminescent Materials and Devices, South China University of Technology, Guangzhou 510640, China
† Equally contributed to this work.
* Corresponding authors (email: yanlingpeng@tyut.edu.cn (Yan L); zgwang2019@sinano.ac.cn (Wang Z); duanchunhui@scut.edu.cn (Duan C); qluo2011@sinano.ac.cn (Luo Q))

ture. P3HT is one of the most classic and cheapest polythiophene donor materials, which plays a key role in the development of OSCs. At present, the highest efficiency of P3HT-based devices is only 11.41% [40]. Recently, we developed a low cost and high-performance polythiophene donor material P5TCN-F25 (as shown in Fig. 1a), and the devices efficiency based on P5TCN-F25 exceeded 17% [41], showing great prospect for low-cost OSCs. Therefore, P5TCN-F25, a promising donor material, was selected in this work. Though the polythiophene-involved OSCs achieved rapid development, the

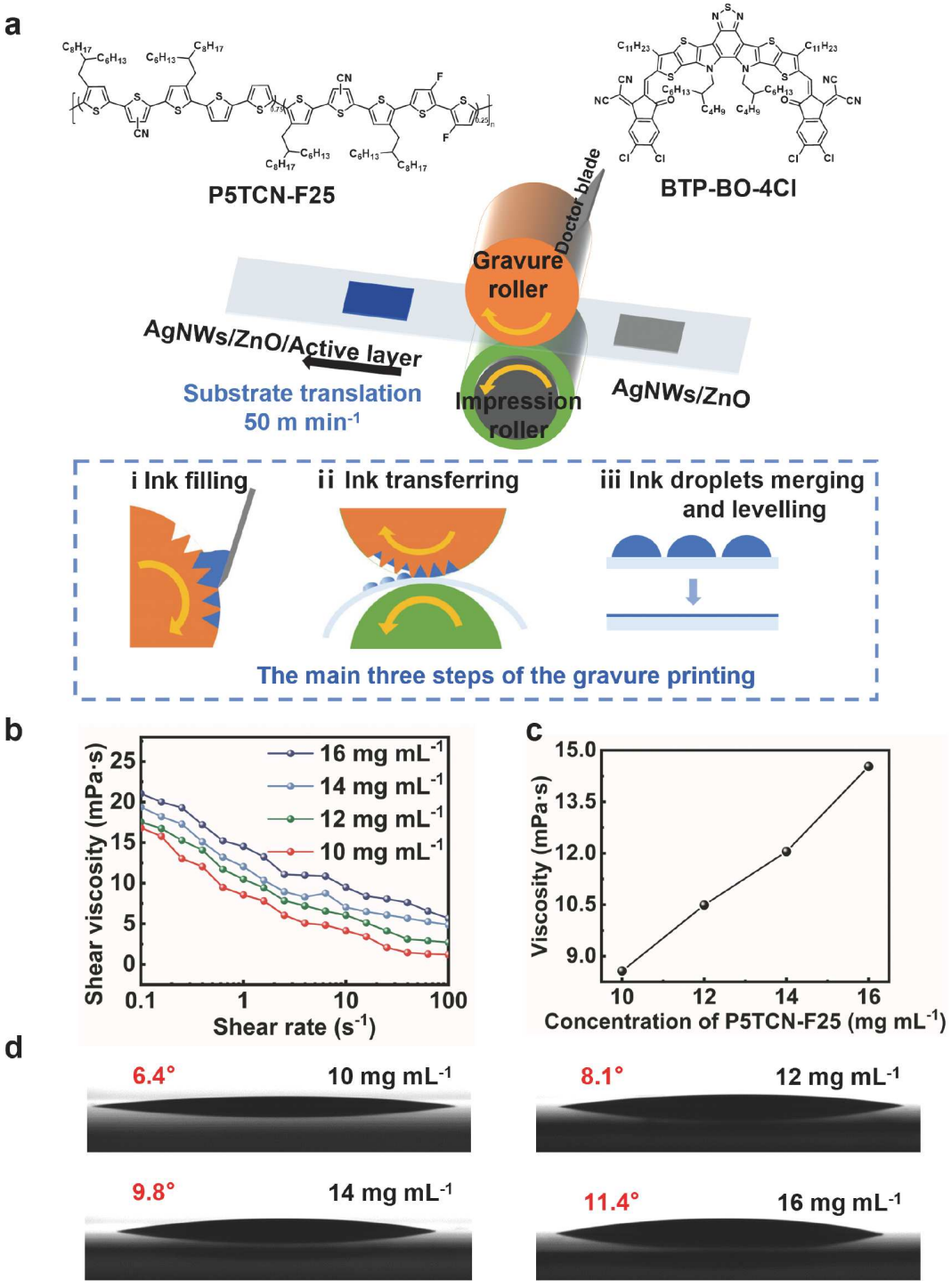

Figure 1 (a) Schematic diagram of the fabrication of PET/AgNWs/ZnO/Active layer films by gravure printing and the three main steps in the gravure process. Insets: i) the doctor blade forces the ink to fill the gravure cavities; ii) the ink is transferred from the cavities of the gravure roller to the substrate; iii) ink droplets level on the substrate. The molecular structure of the active layer donor material P5TCN-F25 and the acceptor material BTP-BO-4Cl. (b) The relationship between shear viscosity and shear rate of active layer inks with different concentrations of P5TCN-F25:BTP-BO-4Cl. (c) The viscosity curve of P5TCN-F25:BTP-BO-4Cl active layer inks with different concentrations (at a shear rate of 1 s^{-1}). (d) The contact angles of the P5TCN-F25 inks on PET/AgNWs/ZnO films at different concentrations. Ink concentrations were 10, 12, 14, and 16 mg mL^{-1}, respectively.

efficiency of printed OSCs with polythiophene materials was limited around 3% [42]. The biggest challenge in preparing OSCs by gravure printing is the uniformity of large-area films [29,43,44], which mainly depends on the rheological properties of the ink, such as viscosity, surface tension, and evaporation rate. The evaporation rate and surface tension of the ink can be easily adjusted by the strategy of mixing solvents and surfactants. However, the viscosity of the active layer ink is usually low and difficult to regulate, which will lead to the poor quality of the gravure printed film, so the regulation of the ink viscosity is a very serious problem for gravure printed active layer films. Thus, excessive aggregation of gravure printed active layer morphology is another important issue.

In this work, low-cost polythiophene (P5TCN-F25) was used as the active layer donor, and the viscosity of ink was adjusted through concentration optimization. With the optimization of the ink viscosity, the random fringes on the printed films were inhibited. In terms of micromorphology, the excessive molecular aggregation was passivated by increasing the temperature of the ink. Ultimately the active layer film with uniform and no obvious streaks was obtained by gravure printing. The PCE of the 1 cm^2 P5TCN-F25:BTP-BO-4Cl flexible OSCs through fully R2R printing reached 10.55%, which was comparable to that of spin-coated devices. This indicates that high-efficiency flexible OSCs can also be fabricated by gravure printing using low-cost polythiophene materials.

EXPERIMENTAL DETAILS

Materials

P5TCN-F25 (M_n = 73 kg mol^{-1}, $Đ_M$ = 1.73) was synthesized according to the procedures reported in previous work [41]. BTP-BO-4Cl was purchased from Hyper Inc. PVP with the molecular weight (M_w) of 13 kg mol^{-1} was purchased from J&K Scientific. ZnO nanoparticles were synthesized as described by Beek *et al.* [45]. AgNW inks (10 mg mL^{-1} in H_2O or isopropyl alcohol with an average diameter of ~25 nm and a length of ~25 μm) were purchased from Nanchang Hechuang Advanced Materials (Nanchang, China). Chlorobenzene (CB, 99.8%) was purchased from J&K Scientific. 1-Chloronaphthalene (CN, 97%) was purchased from TCI. Surface hydrophilic poly ethylene terephthalate (PET) was purchased from Toyobo (Osaka, Japan).

PET/AgNWs/ZnO:PVP film fabrication

PET/AgNWs/ZnO:PVP (PVP: polyvinyl pyrrolidone) films were prepared by the gravure printing method according to our previous report [29]. To obtain the PET/AgNWs-GP electrodes, different formulations were printed on PET substrates using a gravure-printed proof (D&R Lab Gravure Printer G-1100S, Suzhou D&R Instrum Co., Ltd.) at a speed of 50 m min^{-1}. The flexible transparent electrodes were annealed at 120°C for 10 min in an oven. Transparent AgNW electrodes with a sheet resistance of 13 Ω sq^{-1} can be achieved, which were used to for 1 cm^2 OSCs. PVP was dissolved into ethanol to get a PVP solution (10 mg mL^{-1}). The synthesized ZnO NPs were dispersed in butanol solvents (70 mg mL^{-1}). ZnO:PVP ink was obtained by diluting and mixing the two solutions. The concentration of ZnO was 20 mg mL^{-1}, the concentration of PVP was 1 mg mL^{-1}, and the solvent was a mixture of butanol and ethanol with a volume ratio of 1:1 [29]. To obtain the PET/AgNWs/ZnO films, first, the AgNW electrode was treated by the oxygen plasma for 2 min. Then, the ZnO ink was printed on the top of PET/AgNWs electrodes using a gravure-printed proof at a speed of 50 m min^{-1}. The PET/AgNWs/ZnO films were annealed at 120°C for 10 min in an oven.

OSCs fabrication

Flexible OSCs with an inverted PET/AgNWs/ZnO:PVP/P5TCN-F25:BTP-BO-4Cl/MoO_x/Al were fabricated on the PET/AgNWs/ZnO:PVP film. For gravure-printed active layer devices, P5TCN-F25:BTP-BO-4Cl (donor:acceptor (D:A) = 1:1.2; different donor concentrations) was dissolved in CB with the solvent additive of CN (0.25%, *v*/*v*). To obtain the PET/AgNWs/ZnO/P5TCN-F25:BTP-BO-4Cl film, different formulations were printed on PET/AgNWs/ZnO:PVP films using a gravure-printed proof at a speed of 50 m min^{-1}. The flexible PET/AgNWs/ZnO/P5TCN-F25:BTP-BO-4Cl films were annealed at 120°C for 10 min in an oven. For spin-coated active layer devices, P5TCN-F25:BTP-BO-4Cl (D:A = 1:1.2; 14 mg mL^{-1} in concentration of the donor) was dissolved in CB with the solvent additive of CN (0.25%, *v*/*v*). Subsequently, P5TCN-F25:BTP-BO-4Cl was spin-coated at 2000 r min^{-1} for 30 s on the PET/AgNWs/ZnO layer and thermally annealed at 120°C for 10 min. Finally, a MoO_x layer (10 nm) and an Al layer (200 nm) were deposited on the active layer by vacuum evaporation at 5 × 10^{-4} Pa.

Characterization

The viscosity of active layer inks was measured at 25°C using a Malvern Kinexus rheometer (Malvern, UK). The surface tension of active layer inks was measured at 25°C using a Kibron EZ-Piplus Surface Tensiometer (Finland). The photograph of the active layer film prepared by gravure printing was taken with a mobile phone. The roughness of the active layer films was measured using Atomic force microscopy (AFM) (Veeco Dimension 3100, New York, USA) in tapping mode. The Ultraviolet-visible spectroscopy (UV-vis) absorption spectra of the films were obtained by UV-vis spectrophotometer. The thickness of the active layer film was calibrated by step profiler and UV-vis absorption spectroscopy. The sheet resistance of the AgNW electrodes was measured using a ST-2258C four-probe instrument (Suzhou Jingge Electronic, Suzhou, China). The current-voltage (*J*-*V*) measurements were performed in a nitrogen glove box with a Keithley 2400 source meter under simulated AM 1.5 G solar illumination (100 mW cm^{-2}) generated by a Zolix SS150 solar simulator. External quantum efficiency (EQE) values were measured under simulated one sun operation conditions using bias light from a 532-nm solid-state laser (Changchun New Industries, MGL-III-532, China).

RESULTS AND DISCUSSION

Rheological properties of the active layer ink

Fig. 1a shows the schematic diagram of the high-speed preparation process of AgNW electrode, ZnO:PVP electron transporting layer, and active layer by gravure printing. The pattern area of the gravure roller is composed of a uniform cavity structure (as shown in Fig. S1), which gives gravure printing the advantage of preparing a large area of uniform film. The process of gravure printing can be divided into three steps [44,46]. First, through the interaction between the doctor blade and the gravure roller, the ink is filled into the cavities, while the excess ink is removed from the non-pattern region. Then, the ink is

transferred from the cavities of the gravure cylinder to the substrate under the pressure of the impression cylinder and the gravure cylinder. Then, the ink droplets merge and level on the substrate driven by its surface tension. Finally, the solvent volatilizes and inks solidify to form a film. The gravure printing process contains some complex rheological behaviors, so the rheological property of the ink is required to be high, otherwise it will cause uneven film.

In this work, the use of a low-cost polythiophene donor material, P5TCN-F25 [41], combined with low-cost gravure printing technology is expected to significantly reduce the cost of OSCs. The molecular structure of the donor and acceptor used in this work are shown in Fig. 1a. The donor and acceptor have matched energy levels (as shown in Fig. S2), which enable high device performance. In addition, both the donor and acceptor have good processing compatibility in the high boiling solvent, which will be conducive to the preparation through gravure printing.

Then, the influence of ink concentration on the rheological properties of the P5TCN-F25:BTP-BO-4Cl active layer ink was studied (as shown in Fig. 1b, c). It can be seen from the figure that with the increase of ink concentration from 10 to 16 mg mL^{-1}, the viscosity of the ink increases from 8.57 to 14.53 mPa s. This is mainly due to the increase of ink concentration, making the effect of intermolecular entanglement significantly increased. Then, the influence of the ink concentration on the contact angle of the active layer ink on the substrate was further studied and shown in Fig. 1d. It can be seen that the contact angle of the active layer ink on the ZnO film increases from 6.4° to 11.4° with the increase of ink concentration. This is because the viscosity of the ink increases, and the interaction force within the ink increases, increasing the resistance of the ink droplet spreading.

The influence of the ink viscosity on the quality of gravure-printed active layer film and its device performance

The viscosity of the ink was effectively regulated by adjusting the concentration of the ink, and then the influence of the ink viscosity on the film quality was further studied. As shown in Fig. 2a–d, when the concentration of P5TCN-F25 is 10 mg mL^{-1} (the viscosity is 8.57 mPa s), the active layer film of gravure printing has obvious stripes, and the uniformity of the film is very poor. These obvious stripes will cause leakage or even a short circuit of the device. With the increase of the ink viscosity, the formation of stripes was effectively suppressed. This is because the interaction force within the ink is much larger in the high-viscosity inks so that the ink droplets can better adhere on the substrate, which effectively suppresses the flow of inks and the formation of stripes. Then the UV-visible absorption spectra of the printed films at different positions were measured to check the uniformity of the gravure film. As shown in Fig. 2e–h and Fig. S3, the uniformity of the film has been significantly improved with the increase of the ink viscosity.

As we all know, the thickness of the active layer of OSCs plays a key role in the performance of the device, and high-performance devices require appropriate film thickness. Therefore, we

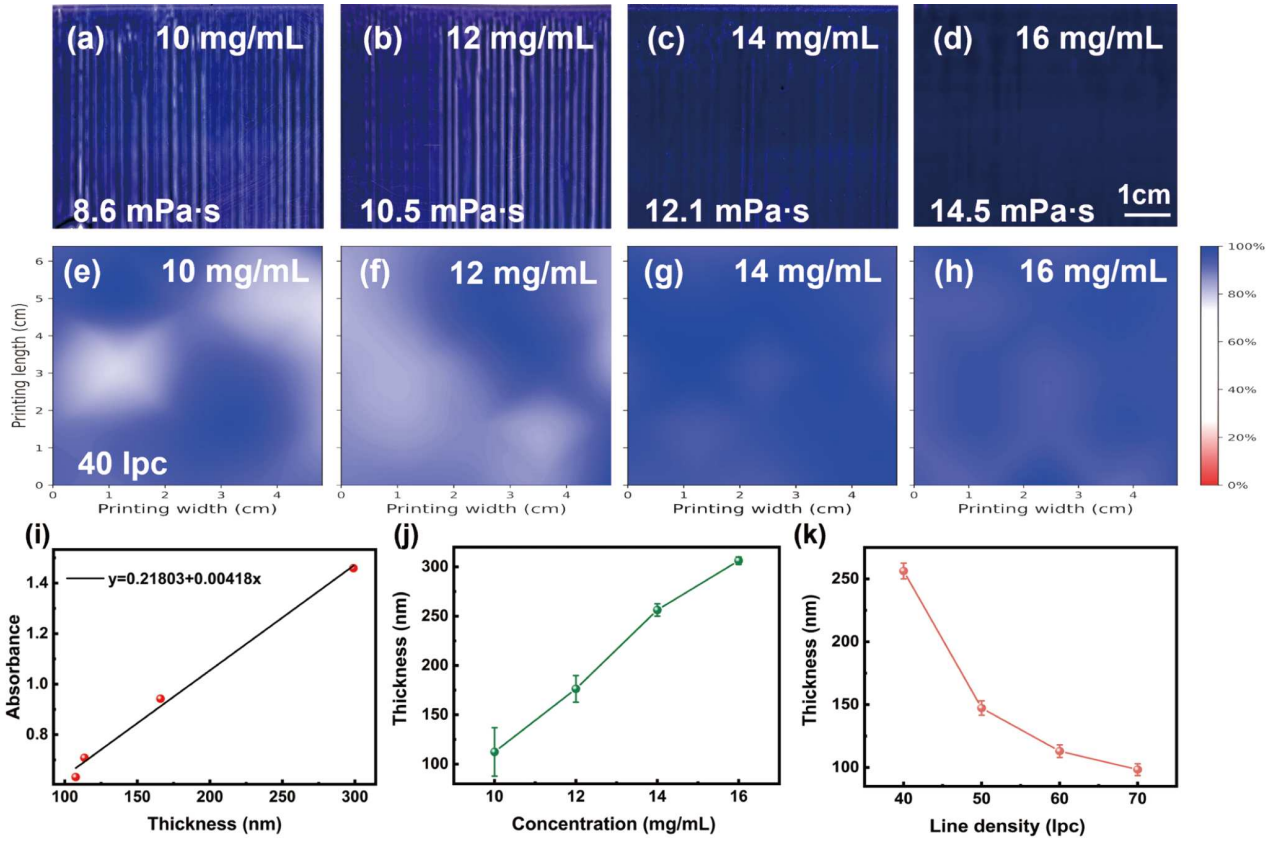

Figure 2 (a–d) The optical images of the bulk-heterojunction (BHJ) films on PET printed from inks with different concentrations, with the line density of 40 lpc, and the printing speed of 50 m min^{-1}. (e–h) The absorption uniformity of the printed films. (i) The relationship between the strength and thickness of the active layer. (j) The correlation of the printed BHJ film thickness *vs.* ink concentration. (k) Gravure-printed active layer thickness *vs.* line density.

used the profilometer combined with the UV-visible light absorption spectrum to characterize the thickness of the gravure-printed active layer film with different ink concentrations (as shown in Fig. 2i–j and Fig. S4a). It can be found that the film thickness gradually increases with the increase of ink concentration. When the concentration is 14 mg mL^{-1}, the film thickness has reached 256 ± 6 nm, which is far beyond the optimal film thickness of the spin coating (100 nm), and too thick an active layer film will affect the carrier transport efficiency. Then, the thickness of the gravure film is reduced by increasing the line density of the gravure roll and reducing the size of the cavities, as shown in Fig. 2i, k and Fig. S4b. The thickness of the gravure film gradually decreases from 256 to 98 nm with the increase of the line density from 40 to 70 line per centimeter (lpc). When the line density of the gravure roller is 60 lpc, the film thickness of 113 nm is nearly the same to the optimal film thickness of the spin-coated devices.

Fig. 3a shows the schematic diagram of the device structure of the gravure-printed OSCs with the device structure of PET/AgNWs/ZnO/P5TCN-F25:BTP-BO-4Cl/MoO_x/Al. Fig. 3b shows the representative *J-V* curves of the gravure-printed and spin-coated cells, and the corresponding cell performance data are shown in Table 1. It can be found that the efficiency of the gravure-printed device is only 9.40%, which is significantly lower than that of the spin-coated device (11.41%). From the statistical distribution diagram of device efficiency (Fig. 3c), the device efficiency distribution range of gravure printing is narrow, indicating that the film of gravure printing has good uniformity. This is because the inks are divided into separate droplets and filled in the uniform cell in gravure printing, which can easily produce a highly uniform film. Fig. 3d shows the EQE curves of the gravure-printed and spin-coated devices, and the EQE integrated current is consistent with the *J-V* test value.

Then, to better understand the effect of exciton dissociation inside the polymer active layer, the relationship between the photocurrent density (J_{ph}) and the effective voltage (V_{eff}) of the flexible devices prepared by gravure printing and spin coating was also studied. As shown in Fig. 3e, the formula $J_{ph} = J_L - J_D$ (where J_L and J_D are current densities under light and darkness, respectively) and $V_{eff} = V_0 - V_{bias}$ are used (where V_0 and V_{bias} are the voltage at $J_{ph} = 0$ and the applied bias voltage, respectively). Under the condition of a short circuit, the exciton dissociation efficiency (P_{diss}) can be calculated according to the formula $P_{diss}=J_{ph}/J_{sat}$. When V_{eff} = 2 V, the carriers are rapidly collected onto the electrode and J_{ph} reaches saturation (J_{sat}). Therefore, the P_{diss}/P_{coll} values of P5TCN-F25:BTP-BO-4Cl based on spin-coated and gravure-printed active layer devices are 98%/78% and 91%/75%, respectively. Spin-coated active layer devices have faster exciton dissociation and higher charge collection efficiency than gravure-printed active layer devices, which may explain the highest J_{SC} performance among devices. These findings reveal the carrier dynamics and recombination processes in P5TCN-F25-based flexible devices, contributing to a better understanding of their performance. For the gravure-printed active layer, the performance loss of flexible devices is serious, which may be related to the microscopic morphology of the active layer film.

Effect of the ink temperature on the morphology of the gravure-printed active layer film and its device performance

Since the efficiency of gravure-printed devices is still significantly decreased compared with that of spin-coated devices,

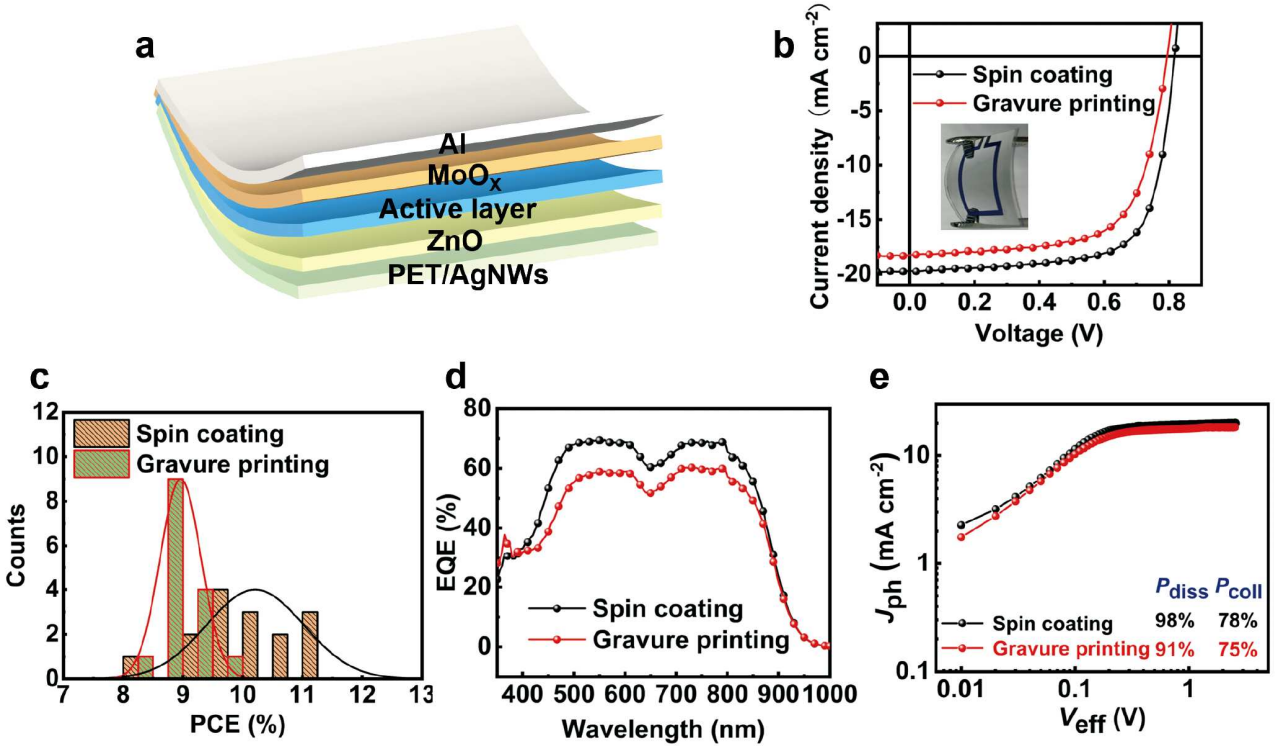

Figure 3 (a) Schematic diagram of the structure of the flexible OSCs. (b) *J-V* curves, (c) Efficiency statistical distributions, (d) EQE curves, and (e) J_{ph}-V_{eff} intensity curves of P5TCN-F25:BTP-BO-4Cl OSCs fabricated by spin-coated and gravure-printed active layers on PET/AgNWs/ZnO film. The ink concentration of the active layer was 14 mg mL^{-1}, and the line density was 60 lpc.

and the material itself has a temperature-dependent aggregation effect [47], we picked three temperatures, which were RT, 70°C and 130°C. We further studied the influence of ink temperature on the film morphology of the gravure-printed active layer, as shown in Fig. 4a–c and Fig. S5. It can be found that the active layer film of gravure printing at RT has obvious aggregation,

Table 1 Device performance of flexible OSCs fabricated by spin-coated and gravure-printed BHJ layers

Deposition method[a]		V_{OC} (V)	J_{SC} (mA cm^{-2})	FF (%)	PCE (%)
Spin coating	Best cell	0.815	19.75	70.09	11.41
	Average[b]	0.797 ± 0.012	19.37 ± 0.54	65.71 ± 3.19	10.27 ± 0.68
Gravure printing	Best cell	0.800	17.74	66.18	9.40
	Average[b]	0.795 ± 0.010	17.65 ± 0.79	64.37 ± 2.43	9.02 ± 0.30

a) The effective area of the device is 1.00 cm^2, and the BHJ layer was coated or printed at room temperature (RT); b) average performance calculated from 12 individual devices.

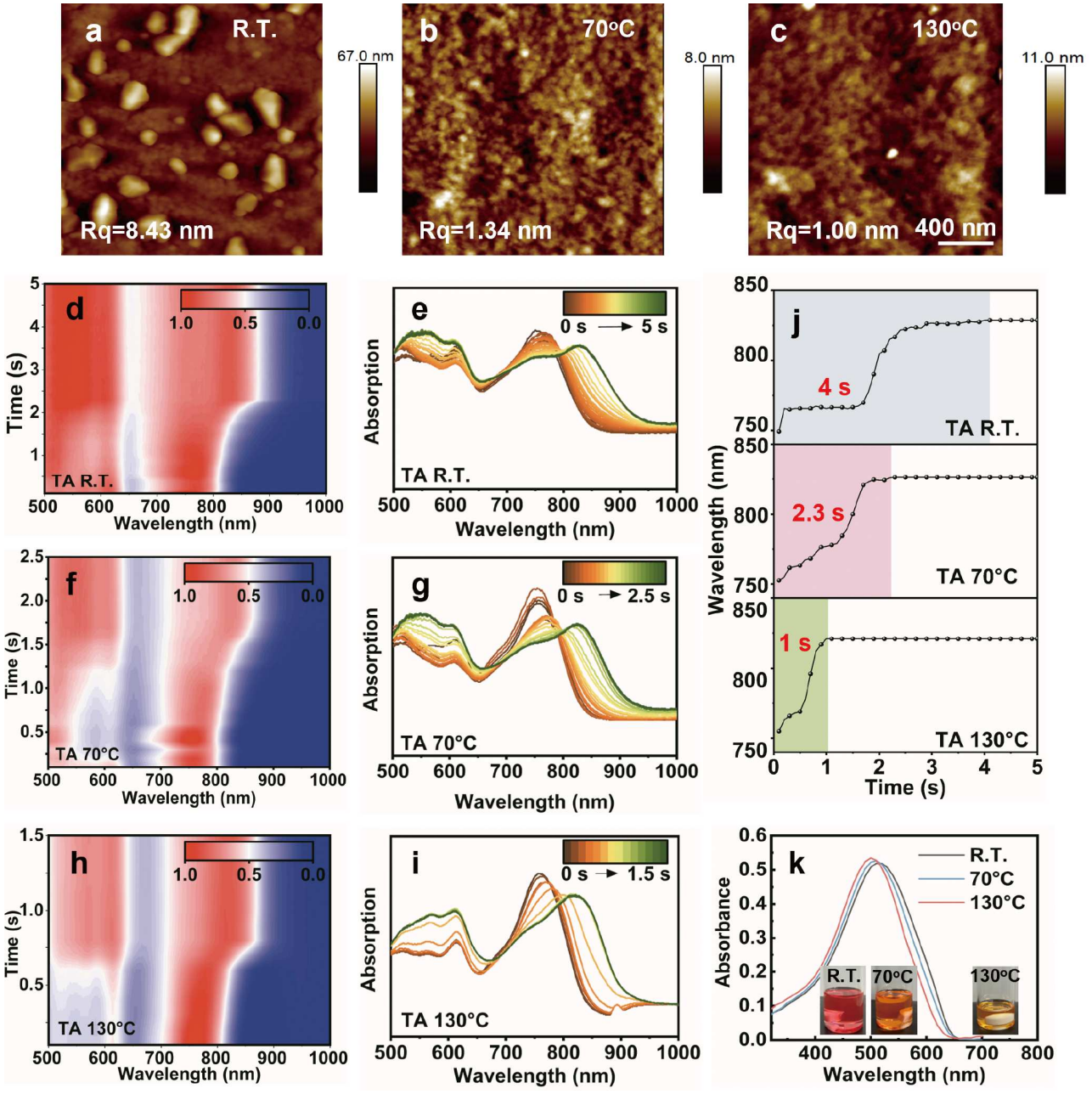

Figure 4 AFM (a–c) height of the active layer gravure-printed on ZnO film with different temperatures of ink. *In-situ* absorption dynamics of gravure-printed active layers and annealing processes at different temperatures, (d, e) RT, (f, g) 70°C. (h, i) 130°C. Annealing temperature: 120°C. The peak position evolution as a function of time of (j) BTP-BO-4Cl in films. (k) The UV-vis absorption spectra of P5TCN-F25 in CB with a concentration of 0.01 mg mL^{-1} under varied temperatures.

which may be the main reason for the degradation of the performance of gravure-printed devices. To solve this problem, we increased the temperature of the ink. When the ink temperature was raised to 70°C, the aggregation on the film was completely suppressed. When the ink temperature was increased to 130°C, the solvent evaporated too quickly, which caused the uniformity of the gravure-printed film.

To better understand the morphology evolution during the gravure printing and annealing process, *in situ* UV–vis absorption spectra were used to study the formation and crystallization kinetics of the blend films. Fig. 4d–i shows the time-resolved absorption spectra and the absorption line profiles of the active layer films processed by gravure printing at RT, 70°C and 130°C, and the location evolution of absorption peaks at representative time points for three films were displayed in Fig. 4j. Obviously, the deposition process of all these films is classified into three stages. Evidently, it represents the solution state, the film formation state, and the film state [48]. The first stage corresponds to the absorption of the solution, which remains the same until the solvents have evaporated. In the second stage, the aggregation process from solution to films. After the film formation, the films reach a stable state and the absorption remains the same at the third stage. Next, the film drying time is extracted for the different temperature solvents.

Compared with the gravure-printed film at RT, 70 and 130°C gravure printing-treated films exhibited shorter film drying times (2.3 s and 1.0 s, respectively). The UV-vis absorption spectra of P5TCN-F25 in CB with a concentration of 0.01 mg mL^{-1} under varied temperatures are displayed in Fig. 4k. P5TCN-F25 presented a blueshift for the intramolecular charge transfer absorption peak as the solution temperature elevated. The solutions were fully disaggregated at RT, 70 and 130°C in CB, respectively. It can also be found that the pre-aggregation state of P5TCN-F25 ink at RT is stronger. Increasing the temperature of the ink can change the aggregation state of the ink and reduce the film drying time, thereby inhibiting the aggregation of the gravure active layer film. The above results indicate that increasing ink temperature can inhibit aggregation, thereby contributing to the optimization of the microscopic active layer morphology and the improvement of charge transport.

Fig. 5a, b shows the *J-V* curves and efficiency distribution histograms of gravure-printed OSCs with different ink temperatures, and the corresponding specific values are shown in Table 2. It can be found that the current and efficiency of gravure-printed devices are improved obviously with the increase in ink temperature. When the ink temperature is at RT, the exciton dissociation efficiency will be significantly reduced due to the large phase size from the excessive aggregation, resulting in a decrease in the device current. When the ink temperature rises to 70°C, the excessive aggregation can be suppressed, thereby improving the exciton dissociation efficiency, and then increasing the device current. When the ink temperature is 70°C, the highest efficiency is 10.55%, and the efficiency loss is only 7.5% compared with that of the spin-coated device. This is mainly because the increase of ink temperature can significantly

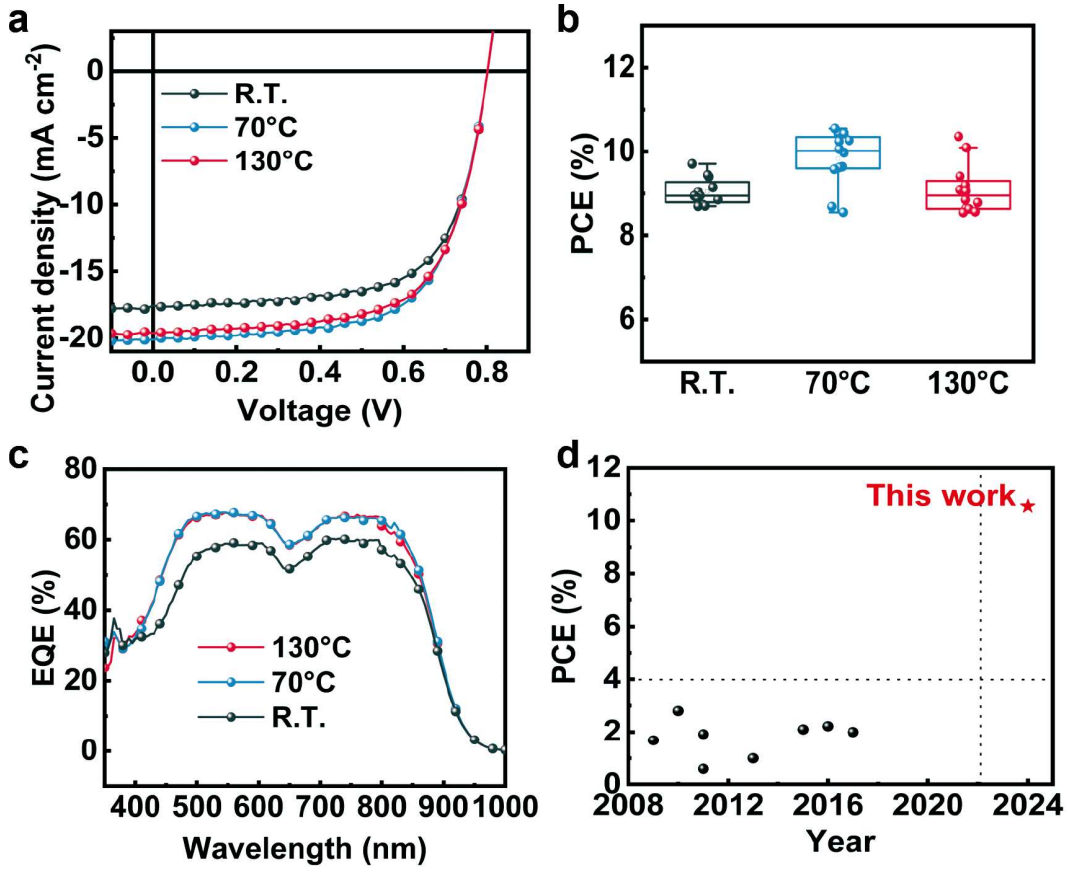

Figure 5 (a) *J-V* curves, (b) efficiency distribution histograms, and (c) EQE curves of fully gravure-printed (three-layer) OSCs prepared at different solution temperatures. (d) Summary of the device efficiency of OSCs fabricated by gravure printing using polythiophene active layer materials in recent years.

Table 2 Device performance[a] of flexible OSCs fabricated by gravure printing active layer inks at different temperatures

Solution temperature (°C)		V_{OC} (V)	J_{SC} (mA cm^{-2})	FF (%)	PCE (%)
RT	Best cell	0.800	17.74	66.18	9.40
	Average[b]	0.795 ± 0.010	17.65 ± 0.79	64.37 ± 2.43	9.02 ± 0.30
70°C	Best cell	0.801	20.07	65.63	10.55
	Average[b]	0.790 ± 0.009	19.15 ± 0.78	64.95 ± 2.13	9.84 ± 0.63
130°C	Best cell	0.800	19.55	66.18	10.36
	Average[b]	0.785 ± 0.009	18.58 ± 0.85	62.47 ± 2.92	9.10 ± 0.57

a) The effective area of the device is 1.00 cm^2, and the BHJ layer was coated or printed at different temperatures; b) average performance calculated from 12 individual devices.

inhibit excessive aggregation and obtain better microscopic morphology, as shown in Fig. 4. Fig. 5c shows the EQE curve of gravure-printed OSCs with different ink temperatures, and the EQE integrated current is consistent with the *J*-*V* test value. To the best of our knowledge, a PCE of 10.55% is the highest value reported in the literature for devices prepared by gravure printing using polythiophene active layer materials (statistical data as shown in Fig. 5d and Table S1 [35–37,42,49–52]). Through this work, the possibility of fabricating high-efficiency flexible OSCs by gravure printing using polythiophene materials is demonstrated.

CONCLUSIONS

In this work, we achieved the gravure printing preparation of large-area, low-cost flexible OSCs based on a low-cost polythiophene donor by regulating the ink properties. The viscosity of the active layer ink was regulated by adjusting the concentration of the ink. The fringes on the gravure-printed active layer film were inhibited obviously, and the film with better homogeneity was obtained. By controlling the ink temperature, the excessive aggregation of gravure-printed active layer film morphology was inhibited, and a better morphology was obtained. Finally, 1 cm^2 flexible OSCs were prepared by gravure printing on PET/AgNWs/ZnO films, and the device efficiency was 10.55%, which was comparable to that of spin-coated devices. This shows that the low-cost polythiophene material system is suitable to be used for the fabrication of high-performance OSCs through gravure printing, which will greatly reduce the cost of organic photovoltaics.

Received 10 August 2024; accepted 10 October 2024; published online 25 November 2024

1 Li Y, Huang X, Sheriff Jr HKM, *et al.* Semitransparent organic photovoltaics for building-integrated photovoltaic applications. Nat Rev Mater, 2022, 8: 186–201
2 Reese MO, Glynn S, Kempe MD, *et al.* Increasing markets and decreasing package weight for high-specific-power photovoltaics. Nat Energy, 2018, 3: 1002–1012
3 Liang Y, Zhang D, Wu Z, *et al.* Organic solar cells using oligomer acceptors for improved stability and efficiency. Nat Energy, 2022, 7: 1180–1190
4 Yuan J, Zhang Y, Zhou L, *et al.* Single-junction organic solar cell with over 15% efficiency using fused-ring acceptor with electron-deficient core. Joule, 2019, 3: 1140–1151
5 Li C, Zhou J, Song J, *et al.* Non-fullerene acceptors with branched side chains and improved molecular packing to exceed 18% efficiency in organic solar cells. Nat Energy, 2021, 6: 605–613
6 Cui Y, Yao H, Zhang J, *et al.* Single-junction organic photovoltaic cells with approaching 18% efficiency. Adv Mater, 2020, 32: 1908205
7 Zhu L, Zhang M, Xu J, *et al.* Single-junction organic solar cells with over 19% efficiency enabled by a refined double-fibril network morphology. Nat Mater, 2022, 21: 656–663
8 Zuo L, Jo SB, Li Y, *et al.* Dilution effect for highly efficient multiple-component organic solar cells. Nat Nanotechnol, 2021, 17: 53–60
9 Cai Y, Li Q, Lu G, *et al.* Vertically optimized phase separation with improved exciton diffusion enables efficient organic solar cells with thick active layers. Nat Commun, 2022, 13: 2369
10 Chen H, Zhang R, Chen X, *et al.* A guest-assisted molecular-organization approach for >17% efficiency organic solar cells using environmentally friendly solvents. Nat Energy, 2021, 6: 1045–1053
11 Ma R, Zhou K, Sun Y, *et al.* Achieving high efficiency and well-kept ductility in ternary all-polymer organic photovoltaic blends thanks to two well miscible donors. Matter, 2022, 5: 725–734
12 Sun Y, Nian L, Kan Y, *et al.* Rational control of sequential morphology evolution and vertical distribution toward 17.18% efficiency all-small-molecule organic solar cells. Joule, 2022, 6: 2835–2848
13 Miao Y, Sun Y, Zou W, *et al.* Isomerization engineering of solid additives enables highly efficient organic solar cells via manipulating molecular stacking and aggregation of active layer. Adv Mater, 2024, 36: 2406623
14 Jiang Y, Dong X, Sun L, *et al.* An alcohol-dispersed conducting polymer complex for fully printable organic solar cells with improved stability. Nat Energy, 2022, 7: 352–359
15 Qin F, Wang W, Sun L, *et al.* Robust metal ion-chelated polymer interfacial layer for ultraflexible non-fullerene organic solar cells. Nat Commun, 2020, 11: 4508
16 Wang Y, Zheng Z, Wang J, *et al.* New method for preparing ZnO layer for efficient and stable organic solar cells. Adv Mater, 2023, 35: e2208305
17 Kan Y, Sun Y, Ren Y, *et al.* Amino-functionalized graphdiyne derivative as a cathode interface layer with high thickness tolerance for highly efficient organic solar cells. Adv Mater, 2024, 36: 2312635
18 Zhu L, Zhang M, Zhou G, *et al.* Achieving 20.8% organic solar cells via additive-assisted layer-by-layer fabrication with bulk p-i-n structure and improved optical management. Joule, 2024, 8: 1–16
19 Zhang T, Xu Y, Yao H, *et al.* Suppressing the energetic disorder of all-polymer solar cells enables over 18% efficiency. Energy Environ Sci, 2023, 16: 1581–1589
20 Ma L, Zhang S, Ren J, *et al.* Design of a fully non-fused bulk heterojunction toward efficient and low-cost organic photovoltaics. Angew Chem Int Ed, 2023, 62: e202214088
21 Li H, Liu S, Wu X, *et al.* Advances in the device design and printing technology for eco-friendly organic photovoltaics. Energy Environ Sci, 2023, 16: 76–88
22 Xue P, Cheng P, Han RPS, *et al.* Printing fabrication of large-area non-fullerene organic solar cells. Mater Horiz, 2022, 9: 194–219
23 Zhao X, Sun R, Wu X, *et al.* High-speed printing of a bulk-heterojunction architecture in organic solar cells films. Energy Environ Sci, 2023, 16: 1711–1720
24 Li M, Zhang K, Qiao J, *et al.* Controlling kinetic quenching depth toward high-performance and photo-stable organic solar cells printed from a non-halogenated solvent. Adv Funct Mater, 2023, 33: 2214361
25 Søndergaard R, Hösel M, Angmo D, *et al.* Roll-to-roll fabrication of

polymer solar cells. Mater Today, 2012, 15: 36–49
26 Krebs FC, Tromholt T, Jørgensen M. Upscaling of polymer solar cell fabrication using full roll-to-roll processing. Nanoscale, 2010, 2: 873–886
27 Ng LWT, Lee SW, Chang DW, *et al.* Organic photovoltaics' new renaissance: advances toward roll-to-roll manufacturing of non-fullerene acceptor organic photovoltaics. Adv Mater Technol, 2022, 7: 2101556
28 Liu Y, Liu B, Ma CQ, *et al.* Recent progress in organic solar cells (Part II device engineering). Sci China Chem, 2022, 65: 1457–1497
29 Wang Z, Guo J, Pan Y, *et al.* Manipulating the macroscopic and microscopic morphology of large-area gravure-printed ZnO films for high-performance flexible organic solar cells. Energy Environ Mater, 2023, 7: e12592
30 Krebs FC. Fabrication and processing of polymer solar cells: A review of printing and coating techniques. Sol Energy Mater Sol Cells, 2009, 93: 394–412
31 Wang G, Adil MA, Zhang J, *et al.* Large-area organic solar cells: material requirements, modular designs, and printing methods. Adv Mater, 2019, 31: 1805089
32 Yang F, Huang Y, Li Y, *et al.* Large-area flexible organic solar cells. npj Flex Electron, 2021, 5: 30
33 Kim YY, Yang TY, Suhonen R, *et al.* Roll-to-roll gravure-printed flexible perovskite solar cells using eco-friendly antisolvent bathing with wide processing window. Nat Commun, 2020, 11: 5146
34 Kim YY, Yang T, Suhonen R, *et al.* Gravure-printed flexible perovskite solar cells: toward roll-to-roll manufacturing. Adv Sci, 2019, 6: 1802094
35 Välimäki M, Jansson E, Korhonen P, *et al.* Custom-shaped organic photovoltaic modules—freedom of design by printing. Nanoscale Res Lett, 2017, 12: 117
36 Kopola P, Aernouts T, Sliz R, *et al.* Gravure printed flexible organic photovoltaic modules. Sol Energy Mater Sol Cells, 2011, 95: 1344–1347
37 Välimäki M, Apilo P, Po R, *et al.* R2R-printed inverted OPV modules – towards arbitrary patterned designs. Nanoscale, 2015, 7: 9570–9580
38 Wang Z, Han Y, Yan L, *et al.* High power conversion efficiency of 13.61% for 1 cm^2 flexible polymer solar cells based on patternable and mass-producible gravure-printed silver nanowire electrodes. Adv Funct Mater, 2021, 31: 2007276
39 Liu Y, Wang Z, Pan Y, *et al.* The influence mechanism of ink viscosity on ink transfer rates and film defects of the roll-to-roll printed organic photoactive layers. Sci China Mater, 2024, 67: 2600–2610
40 Xian K, Ma R, Zhou K, *et al.* Miscibility screening promotes the efficiency and stability of P3HT-based organic solar cells. Aggregate, 2023, 5: e466
41 Yuan X, Zhao Y, Xie D, *et al.* Polythiophenes for organic solar cells with efficiency surpassing 17%. Joule, 2022, 6: 647–661
42 Kopola P, Aernouts T, Guillerez S, *et al.* High efficient plastic solar cells fabricated with a high-throughput gravure printing method. Sol Energy Mater Sol Cells, 2010, 94: 1673–1680
43 Schneider A, Traut N, Hamburger M. Analysis and optimization of relevant parameters of blade coating and gravure printing processes for the fabrication of highly efficient organic solar cells. Sol Energy Mater Sol Cells, 2014, 126: 149–154
44 Hernandez-Sosa G, Bornemann N, Ringle I, *et al.* Rheological and drying considerations for uniformly gravure-printed layers: towards large-area flexible organic light-emitting diodes. Adv Funct Mater, 2013, 23: 3164–3171
45 Beek WJE, Wienk MM, Kemerink M, *et al.* Hybrid zinc oxide conjugated polymer bulk heterojunction solar cells. J Phys Chem B, 2005, 109: 9505–9516
46 Grau G, Cen J, Kang H, *et al.* Gravure-printed electronics: Recent progress in tooling development, understanding of printing physics, and realization of printed devices. Flex Print Electron, 2016, 1: 023002
47 Tan X, Li Y, Yuan X, *et al.* Polythiophene solar cells processed from non-halogenated solvent with 15.68% efficiency. Sci China Chem, 2023, 66: 2347–2353
48 Wang H, Liu S, Li H, *et al.* Green printing for scalable organic photovoltaic modules by controlling the gradient Marangoni flow. Adv Mater, 2024, 36: 2313098
49 Ding JM, de la Fuente Vornbrock A, Ting C, *et al.* Patternable polymer bulk heterojunction photovoltaic cells on plastic by rotogravure printing. Sol Energy Mater Sol Cells, 2009, 93: 459–464
50 Voigt MM, Mackenzie RCI, Yau CP, *et al.* Gravure printing for three subsequent solar cell layers of inverted structures on flexible substrates. Sol Energy Mater Sol Cells, 2011, 95: 731–734
51 Yang J, Vak D, Clark N, *et al.* Organic photovoltaic modules fabricated by an industrial gravure printing proofer. Sol Energy Mater Sol Cells, 2013, 109: 47–55
52 Kapnopoulos C, Mekeridis ED, Tzounis L, *et al.* Fully gravure printed organic photovoltaic modules: A straightforward process with a high potential for large scale production. Sol Energy Mater Sol Cells, 2016, 144: 724–731

Acknowledgement This work was supported by the National Natural Science Foundation of China (22135001, 62404239 and 22475232), Young Cross Team Project of Chinese Academy of Sciences (CAS, JCTD-2021-14), "Dual Carbon" Science and Technology Innovation of Jiangsu province (Industrial Prospect and Key Technology Research program) (BE2022021), and Vacuum Interconnected Nanotech Workstation, Suzhou Institute of Nano-Tech and Nano-Bionics, CAS. This study also received financial support from Guangdong Basic and Applied Basic Research Foundation (2022B1515120008), China Postdoctoral Science Foundation (2023TQ0120, GZB20230223 and 2024M750945) and the Fundamental Research Funds for the Central Universities (2024ZYGXZR063).

Author contributions Yuan X synthesized the polythiophene donor material (P5TCN-F25). Qi W fabricated and performed the characterizations of the flexible OSCs, and analyzed the data. Liu Y measured the AFM images of the printed films. Yang S measured the *in situ* absorption spectra and analyzed the data. Yang S and Chu Y gravure-printed the ZnO electron transport layer together. Qi W and Qian F gravure-printed the silver wire electrodes together. Qi W wrote the manuscript draft. Wang Z, Luo Q, Yuan X, Yan L, and Duan C revised the manuscript. Wang Z, Luo Q, Yan L, and Ma C managed this work. All authors commented and approved the manuscript.

Conflict of interest The authors declare that they have no conflict of interest.

Supplementary information Supplementary materials are available in the online version of the paper.

Weitao Qi is a master student under the guidance of associate Prof. Lingpeng Yan and Prof. Qun Luo. Her main research interest is gravure-printed organic solar cells.

Lingpeng Yan is currently an associate professor at the School of Materials Science and Engineering, Taiyuan University of Technology, where he received his PhD in materials science and engineering in 2017. He was a visiting scholar at the University of Friedrich-Alexander-Universität Erlangen-Nürnberg. His current research interest is in the stability of organic solar cells.

Zhenguo Wang is currently a postdoctoral fellow at Suzhou Institute of Nano-Tech and Nano-Bionics, CAS. He received his PhD from the University of Science and Technology of China in 2023. His current research interest is gravure-printed organic solar cells.

Chunhui Duan received his BS degree from Dalian University of Technology in 2008 and PhD degree from the South China University of Technology in 2013. After a postdoc training at Eindhoven University of Technology, he joined the South China University of Technology as a full professor in 2017. His research interests focus on organic optoelectronic materials and their applications in solar cells, photodetectors, and transistors.

Qun Luo is a professor at Suzhou Institute of Nano-Tech and Nano-Bionics, CAS. She received her PhD degree in materials physics and chemistry in 2011 from Zhejiang University. From January to July, 2011, she did research work in Rennes-1 University of France as a joint PhD. Now, her research interests are flexible, printed thin film photovoltaics and their applications.

基于低成本聚噻吩给体材料的卷对卷凹版印刷有机太阳能电池

祁伟涛[1,2†], 袁熙越[3†], 刘媛琪[2], 杨书涛[2], 储芸莎[2], 钱凡[2], 闫翎鹏[1*], 王振国[2*], 段春晖[3*], 骆群[2*], 马昌期[2]

摘要 目前有机太阳能电池(OSCs)的能量转换效率(PCE)已超过20%, 但大面积低成本有机太阳能电池的发展相对滞后. 实现有机太阳能电池的低成本化, 需要从材料和制备工艺两个方面进行突破; 其中材料方面, 聚噻吩是一种低成本的给体材料; 制备工艺方面, 凹版印刷是一种可二维图案化、高速、高精度和低成本的大面积制备方法. 为了实现低成本的OSCs, 本工作采用低成本的聚噻吩材料为给体材料, 通过卷对卷的凹版印刷技术制备了柔性OSCs. 一方面, 我们通过调节活性层油墨的浓度来调控活性层油墨的粘度, 明显减弱了流动条纹, 获得了均匀的印刷薄膜. 另一方面, 我们通过温度调节, 明显抑制了凹印活性层薄膜微观形貌的过度聚集, 获得了较优的微观形貌. 最终, 通过卷对卷凹版印刷制备1 cm^2的柔性OSCs, 获得了10.55%的器件效率, 与旋涂器件相当. 该结果表明低成本的聚噻吩材料体系可以通过卷对卷凹版印刷的方法制备, 且有望大幅降低有机光伏的生产成本.

